Enhanced energy deposition and carrier generation in silicon induced by two-color intense femtosecond laser pulses

Mizuki Tani [1,*] Kakeru Sasaki,[1] Yasushi Shinohara [1,2] and Kenichi L. Ishikawa [1,2,3,†]

[1]*Department of Nuclear Engineering and Management, Graduate School of Engineering, The University of Tokyo,
7-3-1 Hongo, Bunkyo-ku, Tokyo 113-8656, Japan*

[2]*Photon Science Center, Graduate School of Engineering, The University of Tokyo, 7-3-1 Hongo, Bunkyo-ku, Tokyo 113-8656, Japan*

[3]*Research Institute for Photon Science and Laser Technology, The University of Tokyo, 7-3-1 Hongo, Bunkyo-ku, Tokyo 113-0033, Japan*

We theoretically investigate the optical energy absorption of crystalline silicon subject to dual-color femtosecond laser pulses, using the time-dependent density functional theory. We employ the modified Becke-Johnson exchange-correlation potential, which reproduces the experimental direct band gap energy E_g. We consider situations where one color is in the ultraviolet (UV) range above E_g and the other is in the infrared (IR) range below it. The energy deposition is examined as a function of mixing ratio η of the two colors with the total pulse energy conserved. Energy transfer from the laser pulse to the electronic system in silicon is dramatically enhanced by simultaneous dual-color irradiation and maximized at $\eta \sim 0.5$. The number of generated carriers, not the absorbed energy per carrier, is increased. The effect is more efficient for lower IR photon energy, or, equivalently, larger vector-potential amplitude. The interplay between intraband electron motion in the *valence* band (before excitation) driven by the IR component and resonant valence-to-conduction interband excitation (carrier injection) induced by the UV component is identified as the underlying mechanism. The former increases excitable electrons which pass through the k points of resonant transitions. The effect of different multiphoton absorption paths or intraband motion of carriers generated in the conduction band plays a minor role.

I. INTRODUCTION

The ultrashort laser ablation of semiconductor and dielectric materials [1–4] has been attracting increasing attention due to both broad scientific interest and industrial applications [5,6]. Its advantages include high efficiency and quality [2,7] thanks to the suppression of the heat-affected zone. The laser ablation is initiated by the transfer of optical energy to electrons. Then, irreversible damage is left on the material surface when the energy is subsequently transferred to the lattice [4], the carrier density reaches the critical density at which the plasma frequency is identical to the laser frequency [8], or the interatomic forces are strongly modified owing to massive carrier creation [9–11]. Thus, the fundamental understanding of energy transfer from laser pulses to electrons is critical to further improve the efficiency of laser micromachining [12,13].

There have been studies reporting that the use of synthesized dual-color laser pulse pairs enables highly efficient laser ablation of transparent materials compared to single-color irradiation [14–23]. In Refs. [14,15], the high efficiency observed under dual-color nanosecond ultraviolet (UV) lasers was attributed to the excited-state absorption mechanism, in which the shorter-wavelength component breaks the Si-O covalent bond of fused silica, which increases the absorption efficiency of the longer-wavelength component. References [16,17] reported that the shorter-wavelength laser excites valence electrons into defect or impurity energy levels and that the longer-wavelength laser promotes them from the localized levels to conduction states, even if the former alone cannot directly excite valence electrons into the conduction band. References [18,19] showed that the combination of a picosecond or nanosecond infrared (IR) laser and its second/third harmonics also improves the ablation efficiency of silicon and 3*C*-SiC and attributed it to a mechanism in which the UV laser excites valence electrons into the conduction band, which are then heated by the IR pulse. References [20,21] showed by experiments and analyses based on rate equations that the pair of a femtosecond IR laser and its third harmonic UV can reduce the ablation threshold of fused silica thanks to a defect state that can be reached by single UV photon absorption. It has also been reported that the simultaneous use of a femtosecond IR laser and its second harmonic UV enables efficient laser ablation of polymethylmethacrylate [22] since the synthesized electric field has a larger instantaneous value than in single-color cases. Reference [23] argued, based on experiments and phenomenological modeling, that the modification of sapphire under a femtosecond IR laser and its third harmonics is enhanced

*mzktani@atto.t.u-tokyo.ac.jp
†Corresponding author: ishiken@n.t.u-tokyo.ac.jp

by the contributions of various multiphoton absorption paths, including not only direct valence-conduction ones but also defect-level-mediated ones.

Photoionization in dielectrics under an intense laser pulse has been theoretically modeled by various methods, including the Keldysh theory [24–26], the rate equation [27], the time-dependent Schrödinger equation within the independent electron approximation [28,29], the density matrix method [30–34], and time-dependent density functional theory (TDDFT) [35–39]. By modeling fused silica as a two-level system, González de Alaiza Martínez *et al.* [40] recently claimed that the increase in energy absorption under simultaneous femtosecond IR and UV pulse irradiation is due to the interplay of various multiphoton ionization paths. This argument was supported by Duchateau *et al.* [41] also for a band-dispersion system, α-quartz. Although electron dynamics and high-harmonic generation have been extensively discussed in terms of the coupling between intraband and interband transitions for single-color cases [29,31–33,42–49], the role of the coupling under simultaneous two-color irradiation has been little studied. Thus, while an increase in energy absorption and ablation efficiency by dual-color pulse irradiation appears to be a quite general observation, a consensus has not been reached on its mechanisms, which possibly depend on the materials and irradiation conditions.

In the present study, we investigate the energy absorption by bulk silicon under simultaneous dual-color (UV and IR) femtosecond laser fields, using numerical simulations based on the TDDFT. TDDFT is an *ab initio* framework successfully applied to ultrafast carrier dynamics under intense laser-matter interaction [13,50–57]. We employ the SALMON code [58] and examine the dependence of energy absorption on the mixing ratio η of the two color components with the total intensity (or, equivalently, fluence and energy) conserved. Our calculations show that the absorbed energy is significantly enhanced by dual-color irradiation and maximized at $\eta \sim 0.5$. Our analyses reveal that the intraband motion of the electrons driven in the valence band by the IR field has a substantial role in increasing the valence-to-conduction interband transition induced by the UV field. These observations indicate that the strong-field electron excitation dynamics can be controlled by nonlinear coupling of a long-wavelength-driven intraband motion and a short-wavelength-driven interband transition.

This paper is organized as follows. Section II describes our simulation methods. We briefly review TDDFT and describe how to evaluate absorbed energy. Section III shows the calculated ground state and linear response properties of Si. In Sec. IV we present and analyze our numerical results. Conclusions are given in Sec. V.

II. TIME-DEPENDENT DENSITY FUNCTIONAL THEORY

The time propagation of an N_e-electron system under an optical field is calculated by solving the time-dependent Kohn-Sham equations for the Kohn-Sham orbitals $\{\phi_i(\mathbf{r}, t)\}$ [59],

$$i\hbar \frac{\partial}{\partial t} \phi_i(\mathbf{r}, t) = h_{KS}[n_e(\mathbf{r}, t)]\phi_i(\mathbf{r}, t), \tag{1}$$
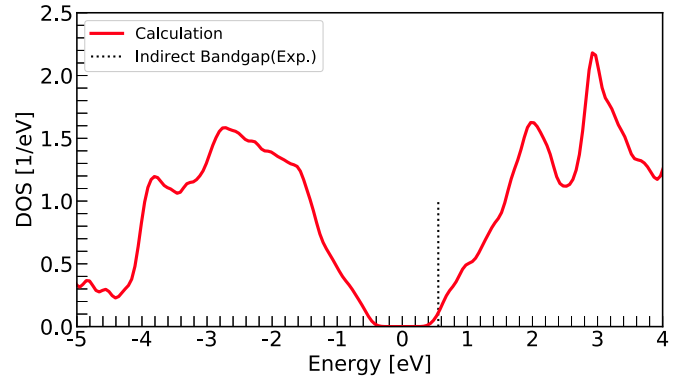

FIG. 1. The calculated density of states of Si (red solid line). The experimental value of the indirect band gap, 1.1 eV [64], is indicated by the vertical black dotted line.

where

$$h_{KS}[n_e(\mathbf{r}, t)] = \frac{1}{2m}[\mathbf{p} + e\mathbf{A}(t)]^2 + V_{eff}[n_e(\mathbf{r}, t)] \tag{2}$$

denotes the velocity gauge Kohn-Sham Hamiltonian within the electric dipole approximation, $\mathbf{p}$ is the canonical momentum, e is the elementary charge, $\mathbf{A}(t)$ is the vector potential, V_{eff} is the effective potential (see below), and m is the electron mass. The time-dependent electron density $n_e(\mathbf{r}, t)$ is given by

$$n_e(\mathbf{r}, t) = 2 \sum_{i \in occ} |\phi_i(\mathbf{r}, t)|^2. \tag{3}$$

The effective potential V_{eff},

$$V_{eff}[n_e(\mathbf{r}, t)] = V_{ion}(\mathbf{r}) + V_H[n_e(\mathbf{r}, t)] + V_{xc}[n_e(\mathbf{r}, t)], \tag{4}$$

consists of the electron-ion potential V_{ion}, which consists of the norm-conserving pseudopotential [60]; the Hartree potential V_H; and the exchange-correlation potential V_{xc}. We employ the modified Becke-Johnson potential [61,62] for V_{xc}.

We consider a two-color pulse whose vector potential $\mathbf{A}(t)$ is described by

$$\mathbf{A}(t) = \mathbf{A}_1(t) + \mathbf{A}_2(t), \tag{5}$$

$$\mathbf{A}_1(t) = -\mathbf{a}_1 \cos^2\left[\frac{\pi}{T}\left(t - \frac{T}{2} - t_{delay}\right)\right]$$
$$\times \sin\left[\omega_1\left(t - \frac{T}{2} - t_{delay}\right)\right]$$
$$\times (t_{delay} \leqslant t \leqslant t_{delay} + T), \tag{6}$$

$$\mathbf{A}_2(t) = -\mathbf{a}_2 \cos^2\left[\frac{\pi}{T}\left(t - \frac{T}{2}\right)\right] \sin\left[\omega_2\left(t - \frac{T}{2}\right)\right]$$
$$\times (0 \leqslant t \leqslant T), \tag{7}$$

where $\mathbf{a}_1$ and $\mathbf{a}_2$ denote the amplitude and polarization vectors of each color, T is the foot-to-foot pulse width (corresponding to 0.36T at FWHM), ω_1 and ω_2 are the central frequencies of each color, and t_{delay} is the time delay between the two colors. $\mathbf{A}_1$ and $\mathbf{A}_2$ are zero vectors outside the time domain of definition ($t < t_{delay}$ or $t > T + t_{delay}$ for $\mathbf{A}_1$, $t < 0$ or $t > T$ for $\mathbf{A}_2$). We set $t_{delay} = 0$ unless explicitly stated otherwise.
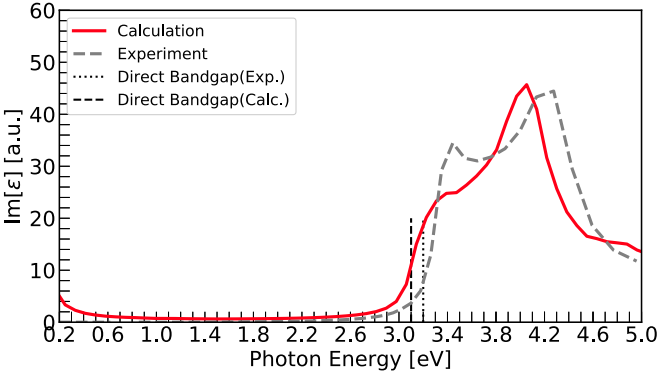
FIG. 2. The calculated imaginary part of the dielectric function of Si (red solid line) and the experimental reference [65] (gray dashed line). The experimental value of the direct band gap, 3.1 eV (3.2 eV [66]), is indicated by the vertical black dashed (black dotted) line.

We evaluate the absorbed energy as work done by the electric field $\mathbf{E}(t) = -\dot{\mathbf{A}}(t)$,

$$W = -e \int_0^T d\tau \mathbf{J}(\tau) \cdot \mathbf{E}(\tau), \qquad (8)$$

with the current density

$$\mathbf{J}(t) = i \frac{2}{\hbar \Omega} \int_\Omega d\mathbf{r} \sum_i \phi_i^*(\mathbf{r}, t)[h_{KS}, \mathbf{r}]\phi_i(\mathbf{r}, t), \qquad (9)$$

where Ω is the volume of the simulation box.

Using the open source package SALMON [58], our simulation is conducted on a crystalline silicon primitive cell (see Appendix A for the crystal structure and the calculated band structure), which is discretized into 16^3 real-space and 16^3 k-space grids. The lattice constant a is set to 5.468 Å (the experimental value is 5.43 Å [63]). The time step is 0.03 a.u., equivalent to 0.7257 as. These parameters are finer than those used in previous works [37,58]. We have also confirmed the convergence of the simulation results (see Appendix B). The laser polarization is assumed to be parallel to the ΓX direction unless specified otherwise.

III. GROUND STATE AND LINEAR RESPONSE

The initial ground state of the system is taken as the eigenstate of the field-free Hamiltonian $h_{KS}|_{\mathbf{A}=\mathbf{0}}$. Figure 1 shows the density of states of the system. The indirect band gap is found to perfectly agree with the experimental one, 1.1 eV [64].

The direct band gap is estimated by the imaginary part of the dielectric function, obtained by time propagation after an impulsive momentum kick. This is realized by a steplike vector potential,

$$\mathbf{A}(t) = \begin{cases} -\mathbf{A}_0 & (t \geqslant 0), \\ 0 & (t < 0), \end{cases} \qquad (10)$$

which corresponds to an impulsive electric field,

$$\mathbf{E}(t) = \mathbf{A}_0 \delta(t). \qquad (11)$$

Noting that the electric field has a constant power spectrum over all frequencies, the diagonal component of the optical
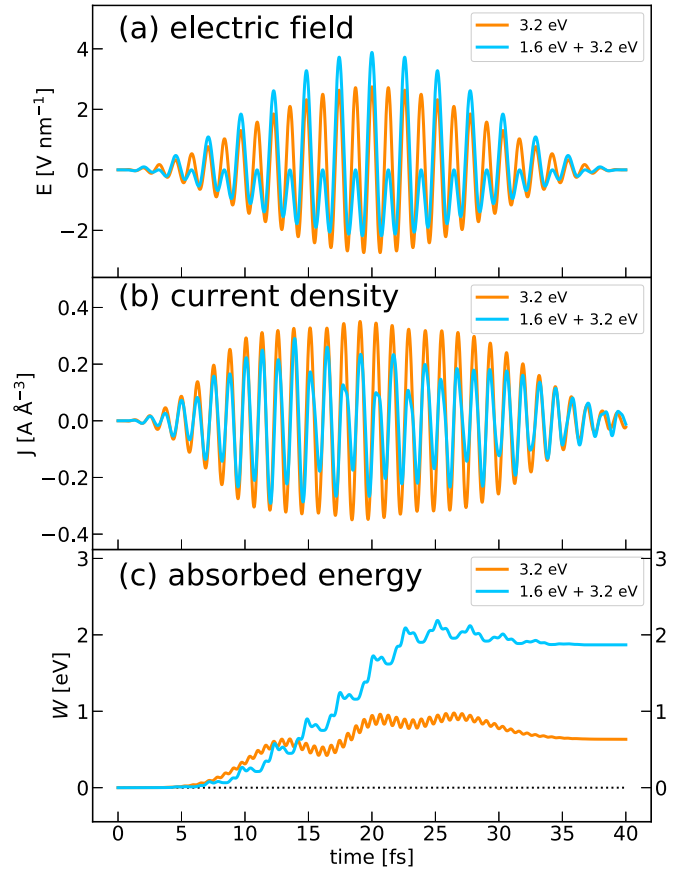

FIG. 3. Temporal profile of (a) the electric field, (b) the calculated current density, and (c) the calculated absorbed energy for $I_{tot} = 10^{12}$ W/cm^2. The orange and cyan solid lines are for the single-color ($\eta = 0$) and dual-color ($\eta = \frac{1}{2}$) fields, respectively.

conductivity is calculated as

$$\sigma_m(\omega) = \frac{-e\hat{J}_m(\omega)}{A_{0m}} \quad (m = x, y, z), \qquad (12)$$

where $\hat{J}_m$ ($m, n = x, y, z$) denotes the m component of the temporal Fourier transform of the current density. Assuming isotropic media, the dielectric function $\varepsilon_m(\omega)$ is given by

$$\varepsilon_m(\omega) = 1 + 4\pi i \frac{\sigma_m(\omega)}{\omega}. \qquad (13)$$

The imaginary part of the thus evaluated dielectric function is consistent with the measured one [65] (Fig. 2). The direct band gap is found to be 3.1 eV, which quasiperfectly agrees with the experimental one, 3.2 eV [66]. The direct energy gap, rather than the indirect one (Fig. 1), is relevant to optical absorption in our calculations. Overall, therefore, the prepared ground state reproduces the electronic properties of real crystalline silicon very well.

IV. RESULTS AND DISCUSSION

A. Energy transfer from laser to electrons

Let us consider energy transfer to silicon from superposed two-color fields with photon energies $\hbar\omega_1$ and $\hbar\omega_2$ ($\hbar\omega_1 \leqslant \hbar\omega_2$), both with a 14.4 fs FWHM pulse width.
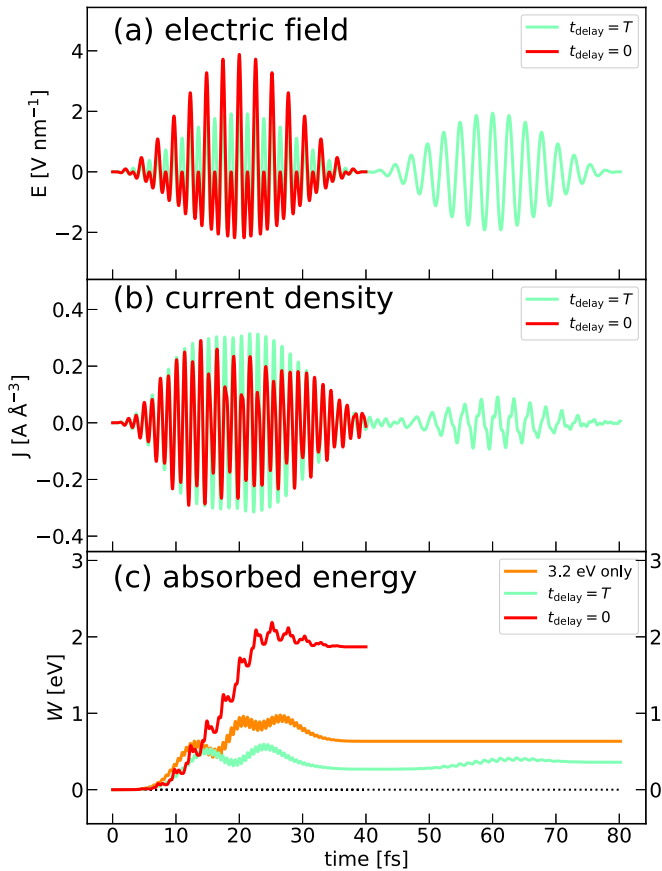
FIG. 4. Temporal profile of (a) the electric field, (b) the calculated current density, and (c) the calculated absorbed energy for $I_{tot} = 10^{12}$ W/cm^2 and $\eta = \frac{1}{2}$. Comparison of simultaneous ($t_{delay} = 0$, red solid line) and delayed ($t_{delay} = T$, lime solid line) dual-color irradiation (1.6 and 3.2 eV). The absorbed energy under a single-color laser field (3.2 eV) is also plotted in (c).

Whereas this pulse width is short compared to those typically used in experiments, computationally demanding TDDFT simulations for such short pulses have been useful to investigate fundamental laser-solid interactions [37,39,41]. We examine how the absorbed energy varies with mixing ratio $\eta = I_1/(I_1 + I_2)$, with I_i ($i = 1, 2$) being the peak intensity of color component i while fixing the total intensity $I_{tot} \equiv I_1 + I_2$. Figure 3 displays the temporal profiles of the electric field, the current density, and the absorbed energy for $\hbar\omega_1 = 1.6$ eV (corresponding to a 775 nm wavelength), $\hbar\omega_2 = 2\hbar\omega_1 = 3.2$ eV (387.5 nm), and $I_{tot} = 10^{12}$ W/cm^2 and compares the results for $\eta = 0$ (only 3.2 eV) and $\frac{1}{2}$ (1.6 and 3.2 eV).

The absorbed energy is significantly (about three times) higher for the two-color case. If we naively assumed an incoherent sum of two-photon excitation by $\hbar\omega_1$ and single-photon ionization by $\hbar\omega_2$, the absorbed energy would scale as $\sigma_1\eta^2 + \sigma_2(1 - \eta)$, with σ_1 (σ_2) being the excitation cross section for $\hbar\omega_1$ ($\hbar\omega_2$), from which we would expect a decrease, rather than an increase, in absorbed energy from two-color mixing. Indeed, if the two pulses are separated in time, energy absorption is significantly reduced and even smaller than in the single-color case (Fig. 4). Thus, simultaneous, rather than consecutive, irradiation is essential to the enhancement.
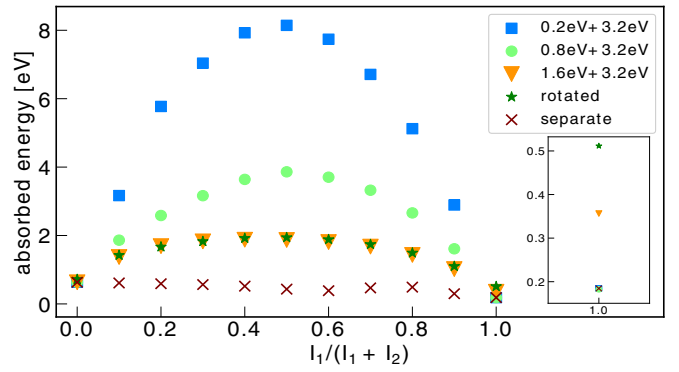

FIG. 5. Absorbed energy as a function of mixing ratio η under $I_{tot} = 10^{12}$ W/cm^2 for three different combinations of $\hbar\omega_1$ and $\hbar\omega_2 = 3.2$ eV indicated in the legend. Green stars: Laser polarizations of both $\hbar\omega_1 = 1.6$ eV and $\hbar\omega_2 = 3.2$ eV are rotated by $\pi/4$. Brown crosses: Delayed irradiation ($t_{delay} = T$) of $\hbar\omega_1 = 0.2$ eV and $\hbar\omega_2 = 3.2$ eV. Inset: Close-up of the results for $\eta = 1$.

Let us further examine the dependence of the absorbed energy on the mixing ratio η, photon energies $\hbar\omega_{1,2}$, laser polarization orientation, and intensity I_{tot}. Figure 5 shows the results as a function of η for $I_{tot} = 10^{12}$ W/cm^2, $\hbar\omega_2 = 3.2$ eV (387.5 nm wavelength), and three different values of $\hbar\omega_1$. Note that $\hbar\omega_2$ (the shorter-wavelength component) is larger than the direct band gap. The green stars in Fig. 5 indicate the transferred energy from the laser field whose polarization is 45° to the ΓX direction; they exhibit almost the same trend as the original laser polarization. Again, combining two colors significantly enhances the energy transfer, maximized at $\eta \sim \frac{1}{2}$. It should be noted that the enhancement effect is larger with smaller $\hbar\omega_1$, or, equivalently, a longer wavelength of the first color, in contrast to the fact that, for $\eta = 1$, the absorbed energy is smaller with smaller $\hbar\omega_1$. Since the longer the wavelength is, the larger the vector-potential amplitude is and thus the crystal-momentum shift of electrons is for a given laser intensity, the results in Fig. 5 indicate that $\hbar\omega_1$ (the longer-wavelength component) contributes to energy absorption predominantly through intraband motion, rather than multiphoton interband excitation. It should be noted that the decomposition into interband and intraband motions is,
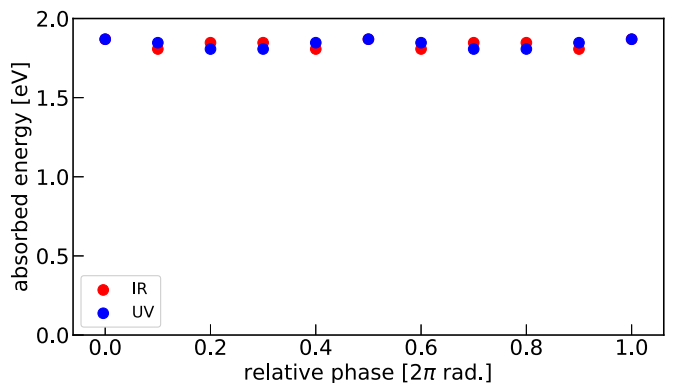

FIG. 6. Relative phase dependence of the absorbed energy. Red (blue) circles indicate that the relative phase of the $\hbar\omega_1 = 1.6$ eV ($\hbar\omega_2 = 3.2$ eV) field is varied with the $\hbar\omega_2$ ($\hbar\omega_1$) phase fixed.
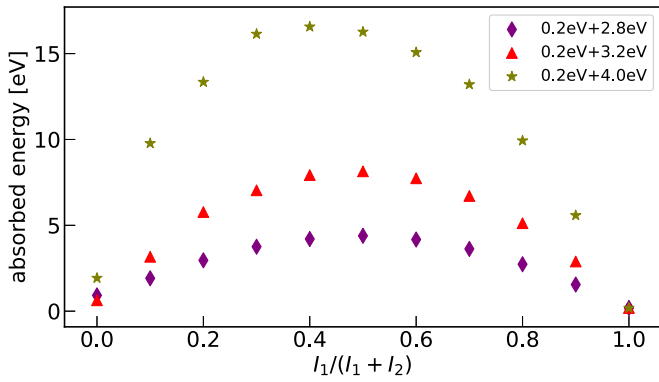
FIG. 7. Absorbed energy as a function of mixing ratio η under $I_{tot} = 10^{12}$ W/cm^2 for the three different combinations of $\hbar\omega_1 = 0.2$ eV and $\hbar\omega_2$ indicated in the legend.

strictly speaking, gauge dependent. Nevertheless, a physical interpretation relying on a particular gauge is often useful, transparent, and valid and gives us clear physical insight. Therefore, in this study, we analyze our simulation results by considering the intraband motion as crystal momentum shift $\mathbf{k}(t) = \mathbf{k}_0 + \mathbf{A}(t)$, with $\mathbf{k}_0$ being its field-free value.

The absorbed energy is nearly independent of the relative phase between the two color fields (Fig. 6). This observation suggests that tunneling ionization is not dominant in the present situation. Indeed, the Keldysh parameter for 1.6 (3.2) eV photon energy and 10^{12} W/cm^2 intensity is 5.3 (10), which corresponds to the multiphoton regime.

In Fig. 7, which plots the absorbed energy vs η for $\hbar\omega_1 = 0.2$ eV (6.2 μm wavelength) and three different values of $\hbar\omega_2$, we can see larger absorption for larger $\hbar\omega_2$ (the shorter-wavelength component), which coincides with the behavior of linear absorption between 2.8 and 4.0 eV (Fig. 2). This observation suggests that the major role of $\hbar\omega_2$ is to induce interband excitation.

In Fig. 8, we display the absorbed energy normalized to the $\hbar\omega_2$-only case ($\eta = 0$) as a function of both I_{tot} and η at $\hbar\omega_1 = 0.2$ eV and $\hbar\omega_2 = 3.2$ eV.

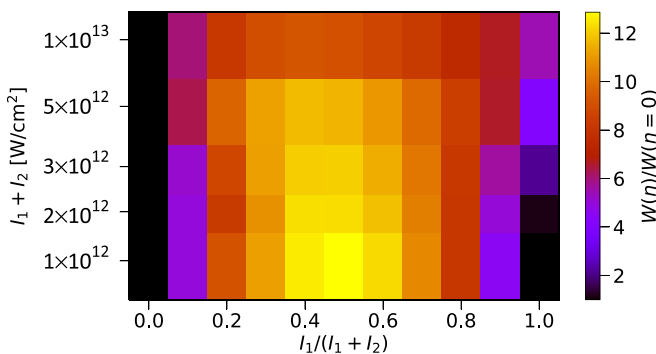The lower intensities exhibit higher maximum-to-minimum contrast (~ 12 for $I_{tot} = 10^{12}$ W/cm^2 and 9

FIG. 8. False-color representation of the absorbed energy normalized to the case $\eta = 0$ [$W(\eta)/W(\eta = 0)$] as a function of mixing ratio η and total peak intensity ($I_1 + I_2 = 10^{12}$–10^{13} W/cm^2) for $\hbar\omega_1 = 0.2$ eV (6200 nm wavelength) and $\hbar\omega_2 = 3.2$ eV (387.5 nm).
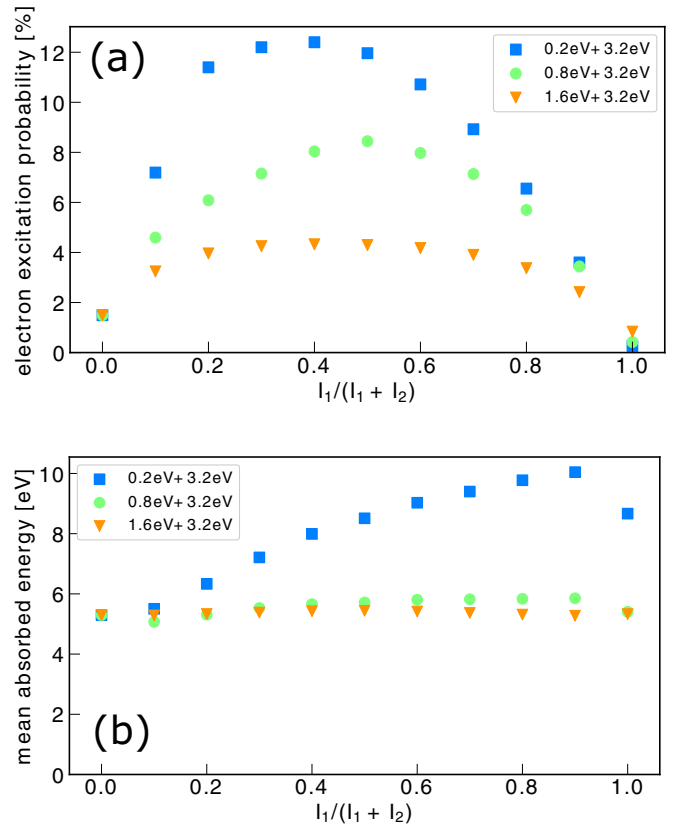

FIG. 9. (a) Fraction of excited electrons and (b) mean absorbed energy per excited electron as a function of mixing ratio η under $I_{tot} = 10^{12}$ W/cm^2 for the three different combinations of $\hbar\omega_1$ and $\hbar\omega_2 = 3.2$ eV indicated in the legend.

for 10^{13} W/cm^2) and symmetric profiles, which become asymmetric with the peak position slightly shifting to the left for higher total intensities. Nevertheless, the absorption is enhanced when both wavelengths are approximately equally mixed, within the intensity range investigated here.

B. Number of excited electrons and mean absorbed energy

The absorbed energy is decomposed into the number of generated carriers (excited electrons) and their mean energy absorption. Then, does an increase in the former or the latter account for the enhanced energy deposition enhancement found in the previous section? To reveal the origin of the energy deposition enhancement under double-color laser fields, we address the η, $\hbar\omega_1$, and $\hbar\omega_2$ dependence of these two quantities. The number of excited electrons n_{ex} is evaluated as

$$n_{ex} = \sum_{i \in \text{cond}} 2 \left| \int d\mathbf{r} \sum_j \phi_i^*(\mathbf{r}, 0) \phi_j(\mathbf{r}, T + t_{\text{delay}}) \right|^2, \quad (14)$$

and the absorbed energy per carrier E_{mean} is

$$E_{\text{mean}} = \frac{W}{n_{ex}}. \quad (15)$$

Figure 9 shows n_{ex} and E_{mean} as a function of the mixing ratio η for $\hbar\omega_2 = 3.2$ eV and three different values of $\hbar\omega_1$.
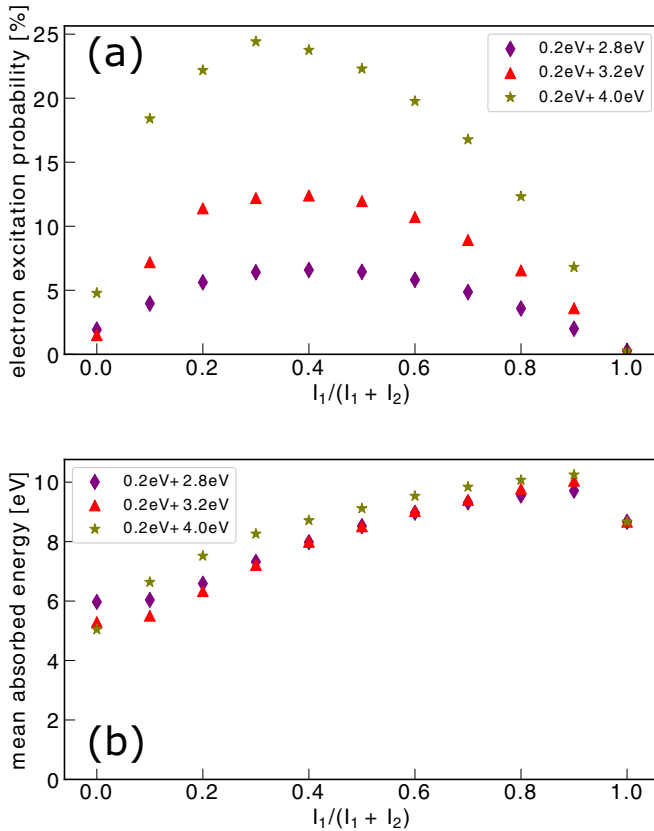
FIG. 10. (a) Fraction of excited electrons and (b) mean absorbed energy per excited electron as a function of mixing ratio η under $I_{\text{tot}} = 10^{12}$ W/cm^2 for the three different combinations of $\hbar\omega_1 = 0.2$ eV and $\hbar\omega_2$ indicated in the legend.

FIG. 11. Temporal evolution of the conduction band population at the Γ, Γ_1, and P points for (a) $\eta = 0$ and (b) $\eta = 0.5$ under $I_{\text{tot}} = 10^{12}$ W/cm^2.

We can see that n_{ex} follows the trend in Fig. 5, strongly enhanced by dual-color irradiation, compared with the single-color cases ($\eta = 0, 1$), peaking at $\eta \sim 0.5$ [Fig. 9(a)]. The enhancement of interband excitation is larger for smaller $\hbar\omega_1$, again consistent with the trend in Fig. 5. On the other hand, the absorbed energy per carrier E_{mean} is surprisingly nearly independent of η for $\hbar\omega_1 = 0.8$ and 1.6 eV [Fig. 9(b)]. Interestingly, E_{mean} is larger than the direct band gap (3.1 eV) because not only the lowest but also higher conduction bands are populated (see Appendix C). For the case of $\hbar\omega_1 = 0.2$ eV, although E_{mean} gradually increases with η, it reaches the maximum at $\eta = 0.9$, rather than $\sim$0.5. Furthermore, the enhancement factor (2 at most) is much smaller than that of W and n_{ex}.

Figures 10(a) and 10(b) display n_{ex} and E_{mean} vs η for $\hbar\omega_1 = 0.2$ eV and three different values of $\hbar\omega_2$, respectively. Again, the number of excited electrons n_{ex} follows a trend similar to that in Fig. 7, peaking at comparable mixing of the two colors and increasing with $\hbar\omega_2$. In contrast, the mean absorbed energy E_{mean} is nearly independent of $\hbar\omega_2$ and only a weak function of η.

Hence, the energy absorption enhanced by two-color pulse irradiation originates mainly from an increase in excitation from the valence to the conduction band, rather than further excitation of carriers generated in the conduction band.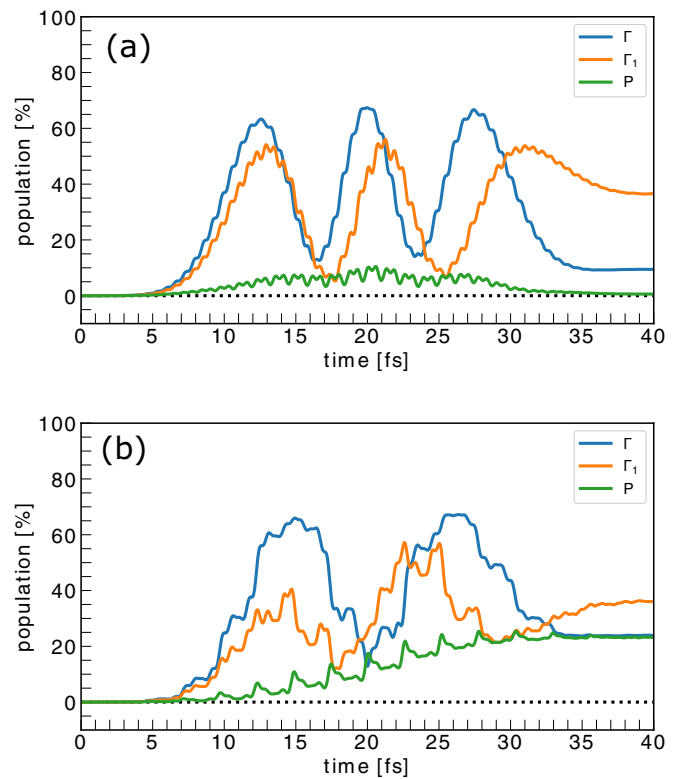 These findings suggest the following mechanism underlying the increased energy absorption under two-color laser fields. The shorter-wavelength component $\hbar\omega_2$ alone would excite only valence electrons of crystal momenta $\mathbf{k}_{\text{res}}$ where $\hbar\omega_2$ is resonant with the excitation energy. In two-color cases, however, the longer-wavelength component $\hbar\omega_1$ drives the intraband motion in the *valence* band; the electronic momentum is shifted as $\mathbf{k}(t) = \mathbf{k}_0 + \mathbf{A}_1(t)$, with $\mathbf{k}_0$ being its field-free value. The peak amplitude of the vector potential $\mathbf{A}_1(t)$ is 0.06431, 0.1286, and 0.5145 a.u. for $\hbar\omega_1 = 1.6, 0.8, 0.2$ eV, respectively, at $I_1 = 5 \times 10^{11}$ W/cm^2. These values should be compared with the half-width of the first Brillouin zone along ΓX, 0.304 a.u. Thus, a substantial part of the valence electrons can pass by the resonant momenta $\mathbf{k}_{\text{res}}$ during the intraband motion, enabling excitation of many more electrons. From the viewpoint of $\hbar\omega_1$, on the other hand, it is much smaller than the band gap, so excitation is not induced much by the longer-wavelength component alone and is facilitated by mixing with the shorter-wavelength component $\hbar\omega_2$. The interplay and balance between the intraband motion by $\hbar\omega_1$ (through vector potential) and interband excitation by $\hbar\omega_2$ (through photon energy) lead to an increase in generated carriers, as in Figs. 9(a) and 10(a), and to maximum enhancement of energy absorption at approximately equal two-color mixing. Interestingly, for the case of $\hbar\omega_1 = 0.2$ eV, the maximum momentum shift (0.5145 a.u.) given by the vector potential amplitude exceeds the Brillouin zone radius. Hence, excited electrons can be shifted in the conduction band to reach the Brillouin zone edge and then further excited to upper bands, which results in increased mean absorbed energy
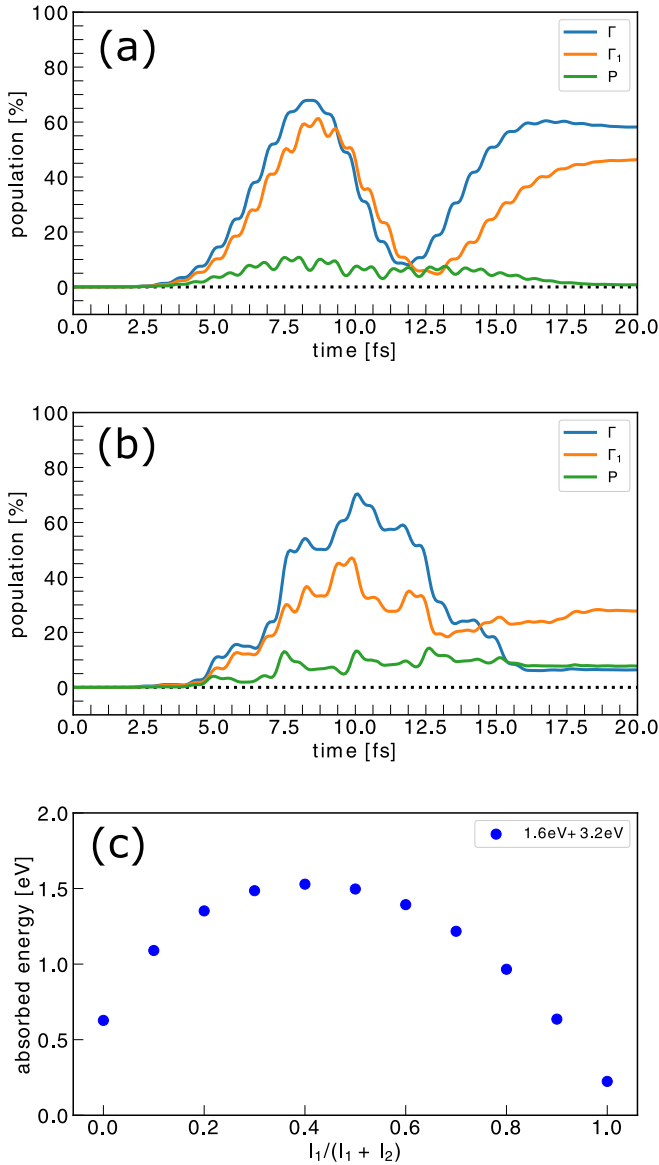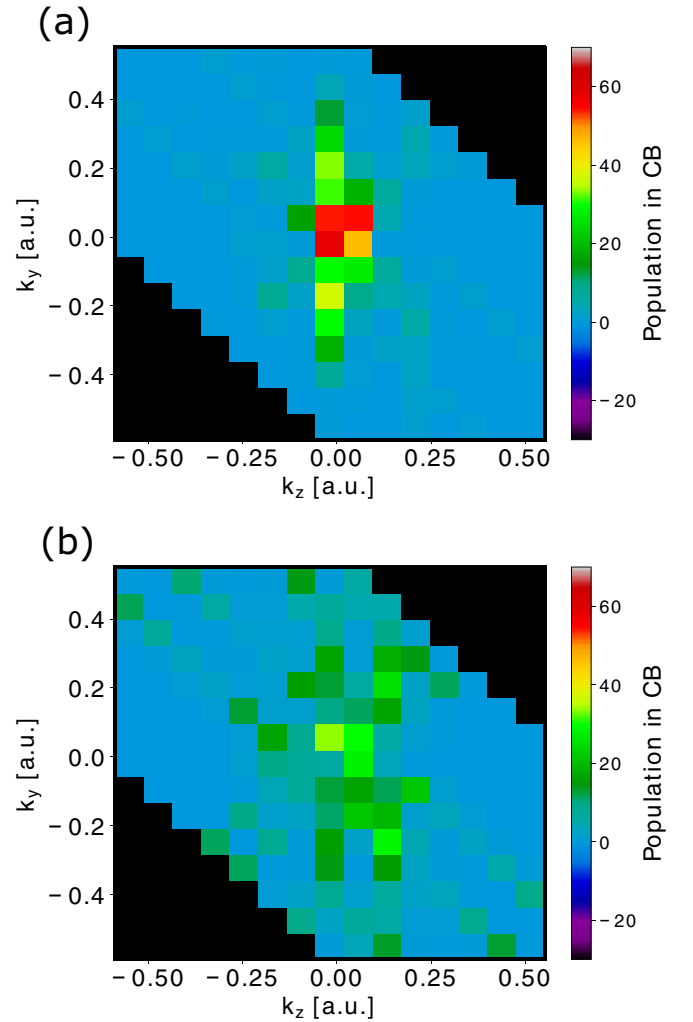
FIG. 13. The residual conduction band population on a cross section ($k_x = -0.019$ a.u.) for (a) $\eta = 0$ and (b) $\eta = 0.5$ under the short pulse (7.2 fs at FWHM, $I_{tot} = 10^{12}$ W/cm^2). Negative values are assigned outside the first Brillouin zone.

FIG. 12. Temporal evolution of the conduction band population at the Γ, Γ_1, and P points for (a) $\eta = 0$ and (b) $\eta = 0.5$ for the case of a 7.2 fs FWHM pulse width. (c) Absorbed energy vs IR mixing ratio η for the case of a 7.2 fs FWHM pulse width. The total peak intensity is $I_{tot} = 10^{12}$ W/cm^2.

[Figs. 9(b) and 10(b)]. It should be emphasized, nevertheless, that the intraband motion in the *valence* band plays a dominant role in the enhanced energy absorption, rather than that in the *conduction* band.

C. Population analysis in k space

To further verify the above-proposed mechanism, we analyze the time-dependent k-resolved population defined by

$$\rho_{\mathbf{k},l}(t) = \left| \int d\mathbf{r} \sum_{m \in \text{occ}} e^{-\frac{i}{\hbar} \int^t d\tau \, \varepsilon_{\mathbf{k}+e\mathbf{A}(\tau),l}} \phi^*_{\mathbf{k}+e\mathbf{A}(t),l}(\mathbf{r}, 0) \phi_{\mathbf{k},m}(\mathbf{r}, t) \right|^2,$$

(16)

$\mathcal{E}$ in Eq. (16) stands for the eigen energy labeled by $\mathbf{k} + e\mathbf{A}(t)$ and l, where l and m denote the band indices. We consider the photon energy combination $\hbar\omega_1 = 1.6$ eV and $\hbar\omega_2 = 3.2$ eV ($I_{tot} = 10^{12}$ W/cm^2) and focus on the following three k points: Γ ($\mathbf{k} = [-0.019, -0.019, -0.019]$), Γ_1 ($\mathbf{k} = [0.019, -0.019, 0.057]$), and P ($\mathbf{k} = [-0.019, -0.019, -0.095]$).

For the case of $\eta = 0.0$ [Fig. 11(a)], the population at and near the Γ point (Γ, Γ_1) exhibits Rabi flopping [45,67], which means the excitation around the Γ point is saturated, while almost no electrons are excited at the P point, which is far from the Γ point. Thus, the energy transfer takes place only around the Γ point, and even there, the laser pulse energy is "wasted." For $\eta = 0.5$ [Fig. 11(b)], on the other hand, while the conduction band is still populated at Γ and Γ_1 as much as for $\eta = 0$, the P point electron is comparably excited. This observation indeed supports our discussion in the previous section that mixing the lower photon energy component into the driving laser field induces intraband motion in the valence band, expressed by the subscript $\mathbf{k} + e\mathbf{A}(t)$ in Eq. (16), and broadens the excitable crystal momentum range, leading to
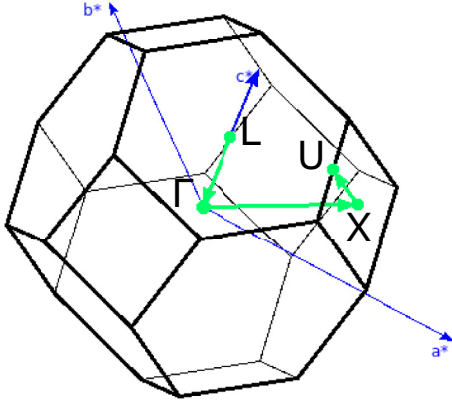
FIG. 14. Wigner-Seitz cell of the crystalline silicon in reciprocal space. The image was generated using XCRYSDEN [72].
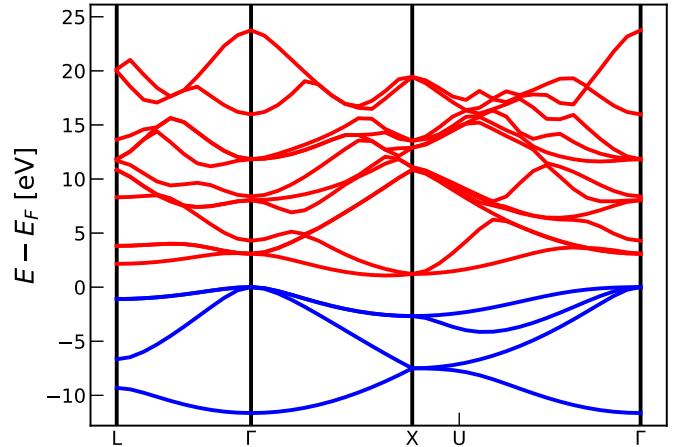

FIG. 15. Energy dispersion for the conduction and valence bands of silicon, calculated using the ABINIT code [70,71] with the lattice constant $a = 5.468$ Å. Red and blue lines indicate conduction and valence bands, respectively.

more efficient use of the laser energy. Although we also see an increase in the residual population even at the Γ point, it happens accidentally during the Rabi oscillation. Indeed, under a shorter pulse (7.2 fs at FWHM, $I_{tot} = 10^{12}$ W/cm^2), the final populations of the Γ and Γ_1 points for $\eta = 0.5$ [Fig. 12(b)] are smaller than for $\eta = 0$ [Fig. 12(a)]. Nevertheless, the absorbed energy is still maximized at $\eta \sim 0.5$ [Fig. 12(c)]. In Fig. 13, we compare the residual population distributions in the conduction band shown as a sectional view along $k_x = -0.019$ a.u. for $\eta = 0.0$ and $\eta = 0.5$ after irradiation with the short laser pulse (7.2 fs at FWHM, $I_{tot} = 10^{12}$ W/cm^2). Again, we find that a wider area of the k space is excited for $\eta = 0.5$ [Fig. 13(b)] than for $\eta = 0.0$ [Fig. 13(a)], leading to higher total excitation probability. These observations indicate that the excitable **k** range expanded by the addition of the longer-wavelength component, not the population transfer at the Γ point alone, makes a major contribution to the enhanced energy absorption.

V. CONCLUSIONS

We have investigated energy absorption by crystalline silicon under two-color laser pulse irradiation by varying the mixing ratio with the total intensity, or, equivalently, fluence fixed to a constant. We have specifically considered the higher photon energy $\hbar\omega_2$ (3.2 eV) in the UV range above the optical gap energy E_g and the lower one $\hbar\omega_1$ (0.2–1.6 eV) in the infrared below it. Our TDDFT computation has shown that energy transfer is substantially enhanced by simultaneous two-color irradiation and is maximized when both color components are roughly equally mixed. The longer the wavelength of the longer-wavelength component is, the more significant the effect is. The increase in carrier generation, rather than that in the absorbed energy per carrier, accounts for the increase in the total absorbed energy. All these observations, along with our k-resolved population analysis, have revealed that the electron dynamics in the valence band driven by the longer-wavelength component $\hbar\omega_1$ plays a crucial role, in contrast to the results in previous studies, which emphasized the interplay of different multiphoton paths or the dynamics of the generated carriers. The $\hbar\omega_2$ field induces interband excitation

(carrier injection) around the Γ point, where the transition energy is resonant with $\hbar\omega_2$. On the other hand, the $\hbar\omega_1$ field of a large vector potential amplitude (corresponding to the maximum momentum shift) drives intraband motion in the valence band, enabling electrons initially far from the Γ point to pass through the resonance, thus extending the excitable k range. Additionally, for the case of $\hbar\omega_1 = 0.2$ eV, the induced momentum shift exceeds the width of the Brillouin zone along ΓX and promotes further excitation of carrier electrons to upper conduction bands.

The decoherence would have some effects depending on dephasing time T_2. Floss *et al.* [68] pointed out that T_2 is of the order of 10 fs, which is longer than the timescale of Rabi oscillation observed in our calculation. Freeman *et al.* [69] recently showed that the relaxation effect on high-harmonic generation emerges only after several tens of femtoseconds. Hence, our simulation results are semiquantitatively valid even in the presence of the decoherence effect.

The degree of ionization and energy per electron are rather high for the photon energy combination (0.2 eV, 3.2 eV).
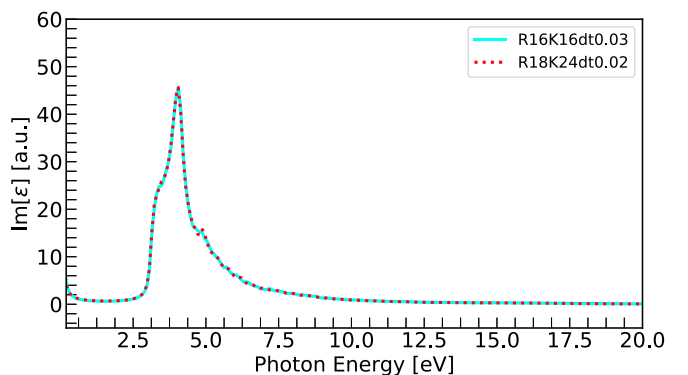

FIG. 16. Imaginary part of the dielectric function using our parameters (light blue solid line) and finer parameters (red dashed line) for real space, k space, and time discretization. See text for the parameter values.
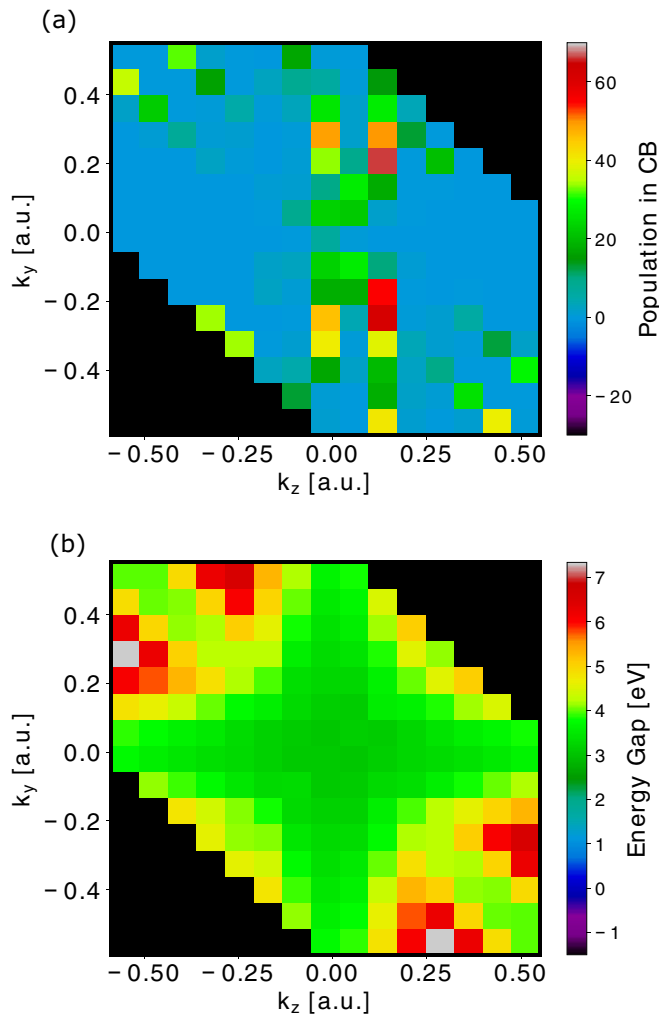
FIG. 17. (a) The residual population of the lowest conduction band on a cross section ($k_x = -0.019$ a.u.) after it is irradiated by the short pulse (7.2 fs at FWHM, $I_{tot} = 10^{12}$ W/cm^2, $\eta = 0.5$). (b) Energy gap between the lowest conduction band and the highest valence band. Negative values are assigned outside the first Brillouin zone.

FIG. 18. (a) The residual population of the second-lowest conduction band on a cross section ($k_x = -0.019$ a.u.) after it is irradiated by the short pulse (7.2 fs at FWHM, $I_{tot} = 10^{12}$ W/cm^2, $\eta = 0.5$). (b) Energy gap between the second-lowest conduction band and the highest valence band. Negative values are assigned outside the first Brillouin zone.

Thus, we should be cautious if we discuss phenomena at a longer timescale, which eventually leads to material processing. On the other hand, in this work, we limit ourselves to the ultrashort timescale before the lattice starts to move significantly. Moreover, the photon energy combination (1.6 eV, 3.2 eV), for which the degree of ionization is 4%, is used in the main part of our analysis. The Rabi oscillation observed in Fig. 11 implies that the band gap is close to the original one, thus indicating that our discussion of the ultrafast electron excitation dynamics based on the ground state band structure is approximately valid and useful for physical understanding of the early stage of laser material processing.

The findings of this work, suggesting dramatic improvement of the femtosecond laser ablation rate of band gap materials, could be experimentally examined using a combination of ultrashort intense midinfrared and ultraviolet laser pulses. Thereby, the increase in the generated carrier will be easier to probe directly rather than the absorbed energy
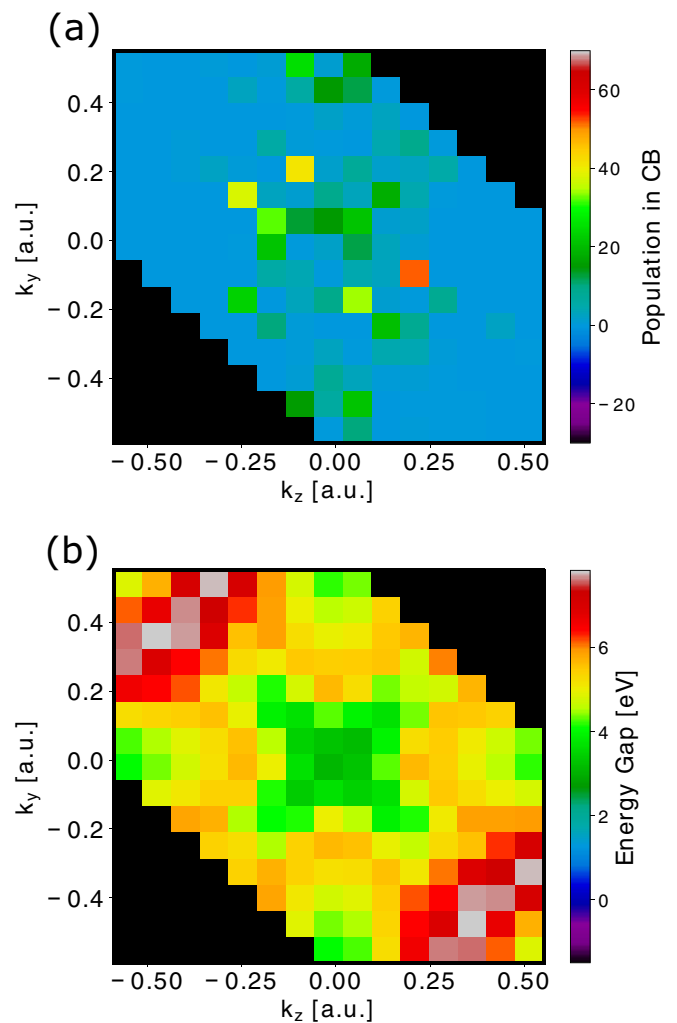
itself. Using a terahertz pulse instead of IR may be even more advantageous since its vector potential has an even larger amplitude.
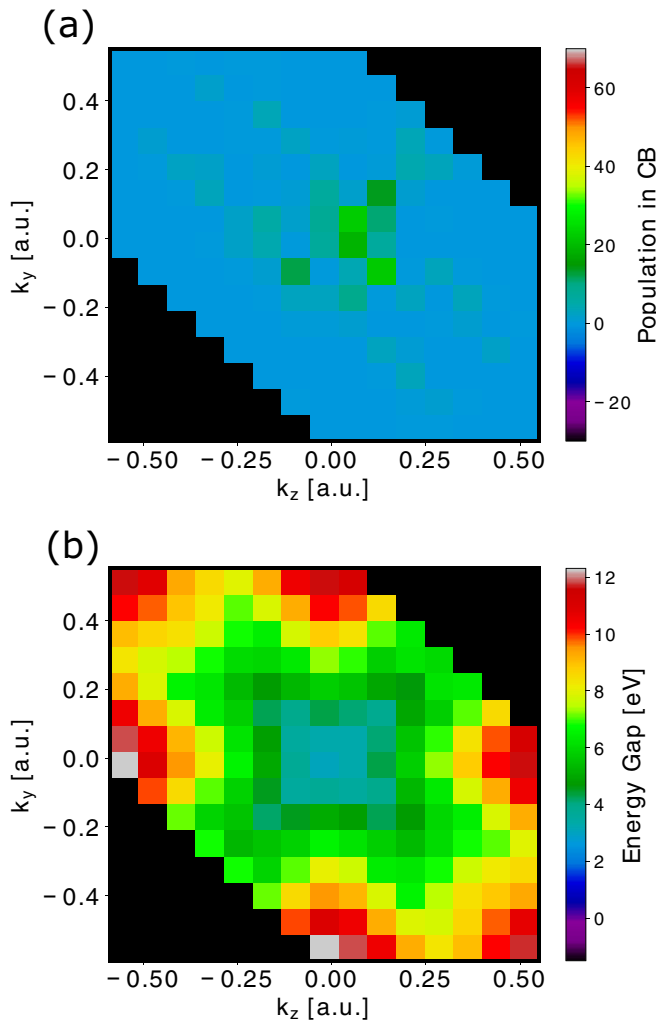
FIG. 19. (a) The residual population of the third-lowest conduction band on a cross section ($k_x = -0.019$ a.u.) after it is irradiated by the short pulse (7.2 fs at FWHM, $I_{tot} = 10^{12}$ W/cm^2, $\eta = 0.5$). (b) Energy gap between the third-lowest conduction band and the highest valence band. Negative values are assigned outside the first Brillouin zone.

APPENDIX A: CRYSTAL STRUCTURE AND BAND STRUCTURE

Figure 14 shows the Wigner-Seitz cell of the crystalline silicon in reciprocal space. Figure 15 shows the energy dispersion of the silicon calculated using the ABINIT code [70,71] with the lattice constant $a = 5.468$ Å.
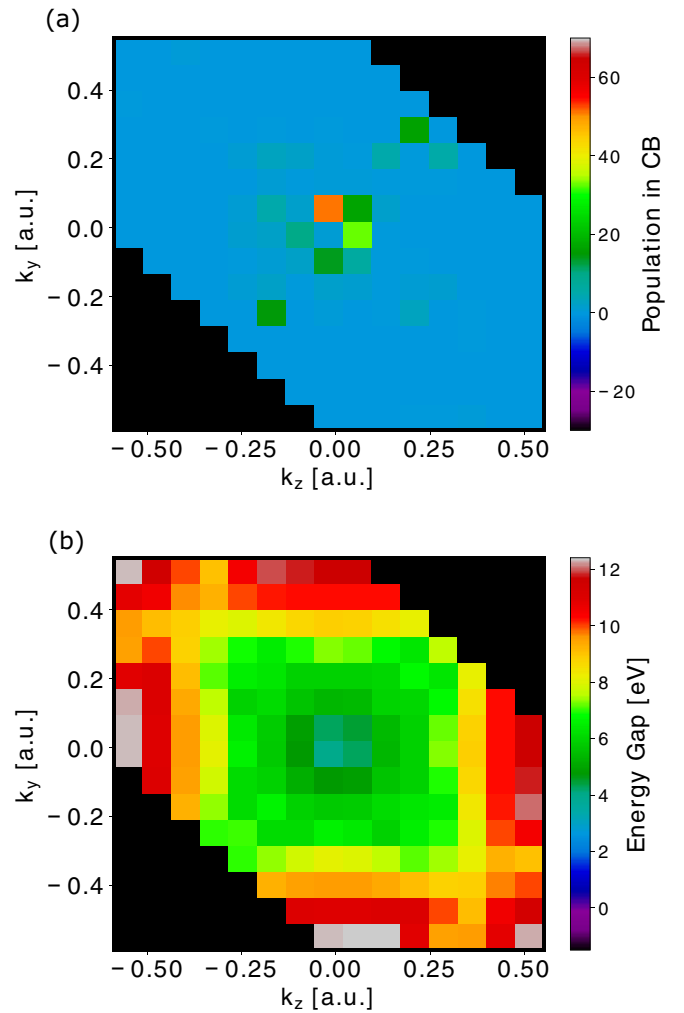
FIG. 20. (a) The residual population of the fourth-lowest conduction band on a cross section ($k_x = -0.019$ a.u.) after it is irradiated by the short pulse (7.2 fs at FWHM, $I_{tot} = 10^{12}$ W/cm^2, $\eta = 0.5$). (b) Energy gap between the fourth-lowest conduction band and the highest valence band. Negative values are assigned outside the first Brillouin zone.

APPENDIX B: CONVERGENCE WITH RESPECT TO GRID SPACINGS AND TIME STEP

Figure 16 compares the imaginary part of the dielectric function Im[ϵ] calculated with two different real- and k-space grid widths and time steps. The red dashed line indicates Im[ϵ] with 16^3 grid points in real space and k space, and the blue line indicates Im[ϵ] with 18^3 grid points in real space and 24^3 grid points in k space. The time step is 0.03 a.u. with the former parameter set and 0.02 a.u. with the latter. The results perfectly overlap, indicating the simulation results are well converged.

APPENDIX C: EXCITED CARRIER POPULATION IN EACH CONDUCTION BAND

Figures 17–20 show the residual population map of each conduction band within the same cross section as in Fig. 13 for $\eta = 0.5$ under $\hbar\omega_1 = 1.6$ eV and $\hbar\omega_2 = 3.2$ eV ($I_1 + I_2 =$

10^{12}W/cm^2) and the energy gap between the valence top band and each conduction band. We see that the electrons are excited around the minimum band gap (3.1 eV) but also at k points where the energy gap is larger than it. Therefore, the mean absorbed energy exceeds the direct band gap [3.1 eV; see Fig. 9(b)].

---

[1] B. N. Chichkov, C. Momma, S. Nolte, F. Von Alvensleben, and A. Tünnermann, Femtosecond, picosecond and nanosecond laser ablation of solids, Appl. Phys. A **63**, 109 (1996).

[2] C. Kerse, H. Kalaycıoğlu, P. Elahi, B. Çetin, D. K. Kesim, Ö. Akçaalan, S. Yavaş, M. D. Aşık, B. Öktem, H. Hoogland, R. Holzwarth, and F. Ö. Ilday, Ablation-cooled material removal with ultrafast bursts of pulses, Nature (London) **537**, 84 (2016).

[3] X. Liu, D. Du, and G. Mourou, Laser ablation and micromachining with ultrashort laser pulses, IEEE J. Quantum Electron. **33**, 1706 (1997).

[4] R. R. Gattass and E. Mazur, Femtosecond laser micromachining in transparent materials, Nat. Photon. **2**, 219 (2008).

[5] K. K. Ostrikov, F. Beg, and A. Ng, Colloquium: Nanoplasmas generated by intense radiation, Rev. Mod. Phys. **88**, 011001 (2016).

[6] K. Sugioka and Y. Cheng, Ultrafast lasers—Reliable tools for advanced materials processing, Light: Sci. Appl. **3**, e149 (2014).

[7] K. Sugioka, Will GHz burst mode create a new path to femtosecond laser processing? Int. J. Extreme Manuf. **3**, 043001 (2021).

[8] J. Thorstensen and S. E. Foss, Temperature dependent ablation threshold in silicon using ultrashort laser pulses, J. Appl. Phys. **112**, 103514 (2012).

[9] A. Rousse, C. Rischel, S. Fourmaux, I. Uschmann, S. Sebban, G. Grillon, P. Balcou, E. Förster, J. P. Geindre, P. Audebert, J. C. Gauthier, and D. Hulin, Non-thermal melting in semiconductors measured at femtosecond resolution, Nature (London) **410**, 65 (2001).

[10] S. K. Sundaram and E. Mazur, Inducing and probing non-thermal transitions in semiconductors using femtosecond laser pulses, Nat. Mater. **1**, 217 (2002).

[11] N. S. Shcheblanov and M. E. Povarnitsyn, Bond-breaking mechanism of vitreous silica densification by IR femtosecond laser pulses, Europhys. Lett. **114**, 26004 (2016).

[12] C. Wang, L. Jiang, F. Wang, X. Li, Y. P. Yuan, and H. L. Tsai, First-principles calculations of the electron dynamics during femtosecond laser pulse train material interactions, Phys. Lett. A **375**, 3200 (2011).

[13] M. Tani, T. Otobe, Y. Shinohara, and K. L. Ishikawa, Semiclassical description of electron dynamics in extended systems under intense laser fields, Phys. Rev. B **104**, 075157 (2021).

[14] K. Sugioka, S. Wada, A. Tsunemi, T. Sakai, H. Takai, H. Moriwaki, A. Nakamura, H. T. H. Tashiro, and K. T. K. Toyoda, Micropatterning of quartz substrates by multi-wavelengthvacuum-ultraviolet laser ablation, Jpn. J. Appl. Phys. **32**, 6185 (1993).

[15] J. Zhang, K. Sugioka, S. Wada, H. Tashiro, and K. Toyoda, Dual-beam ablation of fused quartz using 266 nm and VUV lasers with different delay-times, Appl. Phys. A **64**, 477 (1997).

[16] J. Zhang, K. Sugioka, T. Takahashi, K. Toyoda, and K. Midorikawa, Dual-beam ablation of fused silica by multiwavelength excitation process using KrF excimer and F2 lasers, Appl. Phys. A **71**, 23 (2000).

[17] K. Obata, K. Sugioka, T. Akane, N. Aoki, K. Toyoda, and K. Midorikawa, Influence of laser fluence and irradiation timing of F2 laser on ablation properties of fused silica in F2-KrF excimer laser multi-wavelength excitation process, Appl. Phys. A **73**, 755 (2001).

[18] S. Zoppel, R. Merz, J. Zehetner, and G. Reiderer, Enhancement of laser ablation yield by two color excitation, Appl. Phys. A **81**, 847 (2005).

[19] S. Zoppel, J. Zehetner, and G. A. Reider, Two color laser ablation: Enhanced yield, improved machining, Appl. Surf. Sci. **253**, 7692 (2007).

[20] X. Yu, Q. Bian, Z. Chang, P. B. Corkum, and S. Lei, Femtosecond laser nanomachining initiated by ultraviolet multiphoton ionization, Opt. Express **21**, 24185 (2013).

[21] X. Yu, Z. Chang, P. B. Corkum, and S. Lei, Fabricating nanostructures on fused silica using femtosecond infrared pulses combined with sub-nanojoule ultraviolet pulses, Opt. Lett. **39**, 5638 (2014).

[22] C.-S. Yang, C.-H. Lin, A. Zaytsev, K.-C. Teng, T.-H. Her, and C.-L. Pan, Femtosecond laser ablation of polymethylmethacrylate via dual-color synthesized waveform, Appl. Phys. Lett. **106**, 051902 (2015).

[23] M. Gedvilas, J. Mikšy, J. Berzinš, V. Stankevici, and G. Račiukaitis, Multi-photon absorption enhancement by dual-wavelength double-pulse laser irradiation for efficient dicing of sapphire wafers, Sci. Rep. **7**, 5218 (2017).

[24] L. V. Keldysh, Ionization in the field of a strong electromagnetic wave, Sov. Phys. JETP **20**, 1307 (1965).

[25] N. S. Shcheblanov, M. E. Povarnitsyn, P. N. Terekhin, S. Guizard, and A. Couairon, Nonlinear photoionization of transparent solids: A nonperturbative theory obeying selection rules, Phys. Rev. A **96**, 063410 (2017).

[26] T. Otobe, Y. Shinohara, S. A. Sato, and K. Yabana, Theory for electron excitation in dielectrics under an intense linear and circularly polarized laser fields, J. Phys. Soc. Jpn. **88**, 024706 (2019).

[27] N. Bloembergen, Laser-induced electric breakdown in solids, IEEE J. Quantum Electron. **10**, 375 (1974).

[28] S. Lagomarsino, S. Sciortino, B. Obreshkov, T. Apostolova, C. Corsi, M. Bellini, E. Berdermann, and C. J. Schmidt, Photoionization of monocrystalline CVD diamond irradiated with ultrashort intense laser pulse, Phys. Rev. B **93**, 085128 (2016).

[29] T. Ikemachi, Y. Shinohara, T. Sato, J. Yumoto, M. Kuwata-Gonokami, and K. L. Ishikawa, Trajectory analysis of high-order-harmonic generation from periodic crystals, Phys. Rev. A **95**, 043416 (2017).

[30] M. Lindberg and S. W. Koch, Effective Bloch equations for semiconductors, Phys. Rev. B **38**, 3342 (1988).

[31] K. Kaneshima, Y. Shinohara, K. Takeuchi, N. Ishii, K. Imasaka, T. Kaji, S. Ashihara, K. L. Ishikawa, and J. Itatani, Polarization-Resolved Study of High Harmonics from Bulk Semiconductors, Phys. Rev. Lett. **120**, 243903 (2018).

[32] Y. Sanari, H. Hirori, T. Aharen, H. Tahara, Y. Shinohara, K. L. Ishikawa, T. Otobe, P. Xia, N. Ishii, J. Itatani, S. A. Sato, and

Y. Kanemitsu, Role of virtual band population for high harmonic generation in solids, Phys. Rev. B **102**, 041125(R) (2020).

[33] H. Hirori, P. Xia, Y. Shinohara, T. Otobe, Y. Sanari, H. Tahara, N. Ishii, J. Itatani, K. L. Ishikawa, T. Aharen, M. Ozaki, A. Wakamiya, and Y. Kanemitsu, High-order harmonic generation from hybrid organic-inorganic perovskite thin films, APL Mater. **7**, 041107 (2019).

[34] L. Yue and M. B. Gaarde, Structure gauges and laser gauges for the semiconductor Bloch equations in high-order harmonic generation in solids, Phys. Rev. A **101**, 053411 (2020).

[35] T. Otobe, M. Yamagiwa, J.-I. Iwata, K. Yabana, T. Nakatsukasa, and G. F. Bertsch, First-principles electron dynamics simulation for optical breakdown of dielectrics under an intense laser field, Phys. Rev. B **77**, 165104 (2008).

[36] G. Wachter, C. Lemell, J. Burgdörfer, S. A. Sato, X.-M. Tong, and K. Yabana, *ab initio* Simulation of Electrical Currents Induced by Ultrafast Laser Excitation of Dielectric Materials, Phys. Rev. Lett. **113**, 087401 (2014).

[37] A. Yamada and K. Yabana, Energy transfer from intense laser pulse to dielectrics in time-dependent density functional theory, Eur. Phys. J. D **73**, 87 (2019).

[38] S. Yamada and K. Yabana, Symmetry properties of attosecond transient absorption spectroscopy in crystalline dielectrics, Phys. Rev. B **101**, 165128 (2020).

[39] D. Hui, H. Alqattan, S. Yamada, V. Pervak, K. Yabana, and M. T. Hassan, Attosecond electron motion control in dielectric, Nat. Photonics **16**, 33 (2022).

[40] P. González de Alaiza Martínez, E. Smetanina, I. Thiele, B. Chimier, and G. Duchateau, Modeling the time-dependent electron dynamics in dielectric materials induced by two-color femtosecond laser pulses: Applications to material modifications, Phys. Rev. A **103**, 033107 (2021).

[41] G. Duchateau, A. Yamada, and K. Yabana, Electron dynamics in α-quartz induced by two-color 10-femtosecond laser pulses, Phys. Rev. B **105**, 165128 (2022).

[42] D. Golde, T. Meier, and S. W. Koch, High harmonics generated in semiconductor nanostructures by the coupled dynamics of optical inter- and intraband excitations, Phys. Rev. B **77**, 075330 (2008).

[43] S. Ghimire, A. D. DiChiara, E. Sistrunk, P. Agostini, L. F. DiMauro, and D. A. Reis, Observation of high-order harmonic generation in a bulk crystal, Nat. Phys. **7**, 138 (2011).

[44] C. R. McDonald, G. Vampa, G. Orlando, P. B. Corkum, and T. Brabec, Theory of high-harmonic generation in solids, J. Phys.: Conf. Ser. **594**, 012021 (2015).

[45] M. S. Wismer, S. Y. Kruchinin, M. Ciappina, M. I. Stockman, and V. S. Yakovlev, Strong-Field Resonant Dynamics in Semiconductors, Phys. Rev. Lett. **116**, 197401 (2016).

[46] X.-Q. Wang, Y. Xu, X.-H. Huang, and X.-B. Bian, Interference between inter- and intraband currents in high-order harmonic generation in solids, Phys. Rev. A **98**, 023427 (2018).

[47] S. A. Sato, M. Lucchini, M. Volkov, F. Schlaepfer, L. Gallmann, U. Keller, and A. Rubio, Role of intraband transitions in photocarrier generation, Phys. Rev. B **98**, 035202 (2018).

[48] F. Schlaepfer, M. Lucchini, S. A. Sato, M. Volkov, L. Kasmi, N. Hartmann, A. Rubio, L. Gallmann, and U. Keller, Attosecond optical-field-enhanced carrier injection into the GaAs conduction band, Nat. Phys. **14**, 560 (2018).

[49] X. Song, S. Yang, R. Zuo, T. Meier, and W. Yang, Enhanced high-order harmonic generation in semiconductors by excitation with multicolor pulses, Phys. Rev. A **101**, 033410 (2020).

[50] M. Kozák, M. Martínek, T. Otobe, F. Trojánek, and P. Malý, Observation of ultrafast impact ionization in diamond driven by mid-infrared femtosecond pulses, J. Appl. Phys. **128**, 015701 (2020).

[51] Y. Miyamoto, Direct treatment of interaction between laser-field and electrons for simulating laser processing of metals, Sci. Rep. **11**, 14626 (2021).

[52] T. Otobe, High-harmonic generation in α-quartz by electron-hole recombination, Phys. Rev. B **94**, 235152 (2016).

[53] N. Tancogne-Dejean, O. D. Mücke, F. X. Kärtner, and A. Rubio, Impact of the Electronic Band Structure in High-Harmonic Generation Spectra of Solids, Phys. Rev. Lett. **118**, 087403 (2017).

[54] N. Tancogne-Dejean, M. A. Sentef, and A. Rubio, Ultrafast Modification of Hubbard U in a Strongly Correlated Material: *ab initio* High-Harmonic Generation in NiO, Phys. Rev. Lett. **121**, 097402 (2018).

[55] N. Tancogne-Dejean and A. Rubio, Atomic-like high-harmonic generation from two-dimensional materials, Sci. Adv. **4**, eaao5207 (2018).

[56] I. Floss, C. Lemell, K. Yabana, and J. Burgdörfer, Incorporating decoherence into solid-state time-dependent density functional theory, Phys. Rev. B **99**, 224301 (2019).

[57] S. Yamada and K. Yabana, Determining the optimum thickness for high harmonic generation from nanoscale thin films: An *ab initio* computational study, Phys. Rev. B **103**, 155426 (2021).

[58] M. Noda, S. A. Sato, Y. Hirokawa, M. Uemoto, T. Takeuchi, S. Yamada, A. Yamada, Y. Shinohara, M. Yamaguchi, K. Iida, I. Floss, T. Otobe, K.-M. Lee, K. Ishimura, T. Boku, G. F. Bertsch, K. Nobusada, and K. Yabana, SALMON: Scalable *ab-initio* light–matter simulator for optics and nanoscience, Comput. Phys. Commun. **235**, 356 (2019).

[59] E. Runge and E. K. U. Gross, Density-Functional Theory for Time-Dependent Systems, Phys. Rev. Lett. **52**, 997 (1984).

[60] M. Fuchs and M. Scheffler, *Ab initio* pseudopotentials for electronic structure calculations of poly-atomic systems using density-functional theory, Comput. Phys. Commun. **119**, 67 (1999).

[61] F. Tran and P. Blaha, Accurate Band Gaps of Semiconductors and Insulators with a Semilocal Exchange-Correlation Potential, Phys. Rev. Lett. **102**, 226401 (2009).

[62] S. A. Sato, Y. Taniguchi, Y. Shinohara, and K. Yabana, Nonlinear electronic excitations in crystalline solids using meta-generalized gradient approximation and hybrid functional in time-dependent density functional theory, J. Chem. Phys. **143**, 224116 (2015).

[63] E. Massa, G. Mana, U. Kuetgens, and L. Ferroglio, Measurement of the lattice parameter of a silicon crystal, New J. Phys. **11**, 053013 (2009).

[64] P. J. Collings, Simple measurement of the band gap in silicon and germanium, Am. J. Phys. **48**, 197 (1980).

[65] C. Schinke, P. C. Peest, J. Schmidt, R. Brendel, K. Bothe, M. R. Vogt, I. Kröger, S. Winter, A. Schirmacher, S. Lim, H. T. Nguyen, and D. MacDonald, Uncertainty analysis for

the coefficient of band-to-band absorption of crystalline silicon, AIP Adv. **5**, 067168 (2015).

[66] D. E. Aspnes and A. A. Studna, Dielectric functions and optical parameters of Si, Ge, GaP, GaAs, GaSb, InP, InAs, and InSb from 1.5 to 6.0 eV, Phys. Rev. B **27**, 985 (1983).

[67] X. G. Zhao, G. A. Georgakis, and Q. Niu, Rabi oscillations between Bloch bands, Phys. Rev. B **54**, R5235 (1996).

[68] I. Floss, C. Lemell, G. Wachter, V. Smejkal, S. A. Sato, X.-M. Tong, K. Yabana, and J. Burgdörfer, *ab initio* multiscale simulation of high-order harmonic generation in solids, Phys. Rev. A **97**, 011401(R) (2018).

[69] D. Freeman, A. Kheifets, S. Yamada, A. Yamada, and K. Yabana, High-order harmonic generation in semiconductors driven at near- and mid-infrared wavelengths, Phys. Rev. B **106**, 075202 (2022).

[70] X. Gonze *et al.*, The abinitproject: Impact, environment and recent developments, Comput. Phys. Commun. **248**, 107042 (2020).

[71] A. H. Romero *et al.*, ABINIT: Overview and focus on selected capabilities, J. Chem. Phys. **152**, 124102 (2020).

[72] A. Kokalj, Computer graphics and graphical user interfaces as tools in simulations of matter at the atomic scale, Comput. Mater. Sci. **28**, 155 (2003).